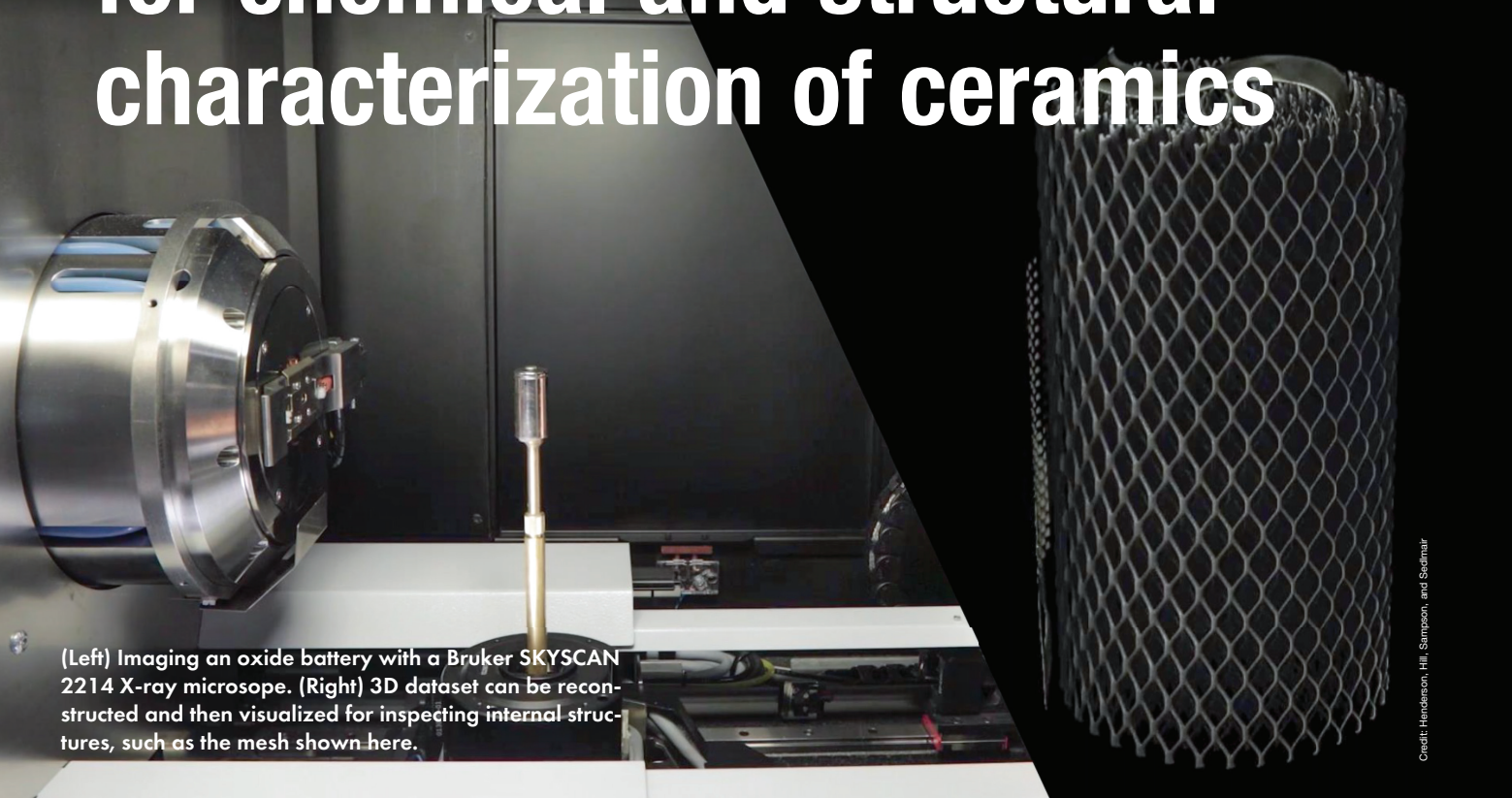


Analytical X-ray techniques for chemical and structural characterization of ceramics



(Left) Imaging an oxide battery with a Bruker SKYSCAN 2214 X-ray microscope. (Right) 3D dataset can be reconstructed and then visualized for inspecting internal structures, such as the mesh shown here.

Credit: Henderson, Hill, Sampson, and Sedlmair

By Nathan Henderson, Tina Hill, David Sampson, and Julia Sedlmair

X-ray techniques are key instrumental methods for chemical and structural analysis of ceramics. This article provides a high-level overview of several analytical X-ray technologies.

Materials testing is essential to qualifying ceramics at various stages of the production cycle—from raw materials verification to characterizing finished formed parts.

In this article, we highlight several key instrumental methods for chemical and structural analysis of ceramics: X-ray fluorescence in both bulk- and microscale applications (XRF and μ XRF, respectively), powder X-ray diffraction (XRD), and X-ray microscopy (XRM).

XRF measurements provide information regarding chemical and elemental composition and can be used in both qualitative and quantitative experiments. Bulk XRF methods are used to test raw feedstocks to verify reagent purity and the desired ratios in intermediate and final products. μ XRF provides similar information within a constrained physical area, allowing for elemental mapping of parts and surfaces. XRD can identify

and quantify crystalline polymorphs by distinguishing between different packing arrangements of atomic and molecular species. Finally, XRM is an imaging technique that explores internal structure and allows for the characterization of features such as cracks and defects.

We will discuss each technique in the following sections, providing a high-level overview of the method as well as relevant examples of the types of data one can expect from an experiment. Additionally, we will describe a case study that uses multiple techniques for a more thorough sample analysis.

X-ray fluorescence

XRF spectrometry plays a crucial role in the ceramics industry for process control and contamination tracing. It enables rapid, nondestructive elemental analysis, ensuring products meet quality standards.

By monitoring elemental composition in real-time, manufacturers can optimize production conditions and detect deviations early in the process. The sensitivity of XRF allows for the identification of contaminants and unknown materials, contributing to quality assurance. The nondestructive nature of XRF makes it a cost-effective and efficient tool for assessing ceramic composition and maintaining product consistency throughout the manufacturing process.

In an XRF experiment, information about the elemental composition of a material is produced through the interactions of a sample and a beam of X-rays. One interaction that occurs is a core electron (K or L shell) is freed by the incident

beam, and the vacancy is filled by the transition of an outer shell electron. These transitions result in the generation of fluorescent photons with characteristic energies that can be used to identify distinct elements, much like a fingerprint. X-rays can also be scattered by the material via elastic (Rayleigh) or inelastic (Compton) processes without core electron interactions, yielding information about the general matrix.

For ceramics, this technique is used to quantify raw materials and additives; determine ratios of major compounds; screen for impurities; and for specialized tasks, such as determining coating thickness. Following elemental identification, quantification can be achieved through use of a calibration curve or by modeling with fundamental parameters. With respect to precision, repetition studies typically demonstrate standard deviations of less than 0.5 rel.% for major compounds, less than 1 rel.% for minor compounds, and down to the single digit parts per million (ppm, absolute) for trace amounts.

XRF instrumentation can be categorized as either energy dispersive (ED-XRF) or wavelength dispersive (WD-XRF), with some differences in components and detection (Figure 1). ED-XRF acquires wide-range spectra during a measurement. There are few moving parts, and it is often used for fast, routine measurements in quality control environments. Current state-of-the-art 8k detectors differentiate between the most common elements.

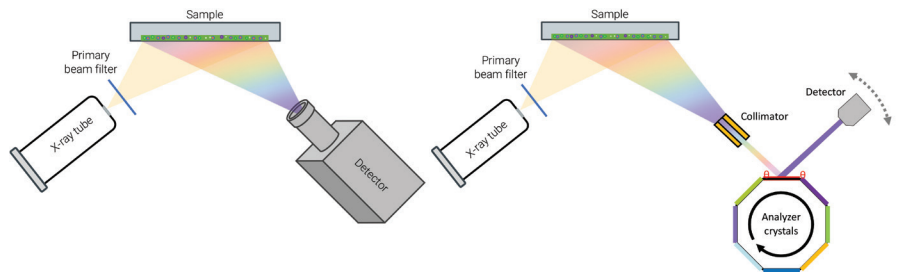


Figure 1. Schematic highlighting the difference between ED-XRF (left) and WD-XRF (right). ED-XRF instruments collect wide energy spectra while WD-XRF instruments have additional components in the beam path and higher energy, which allow for increased resolution.

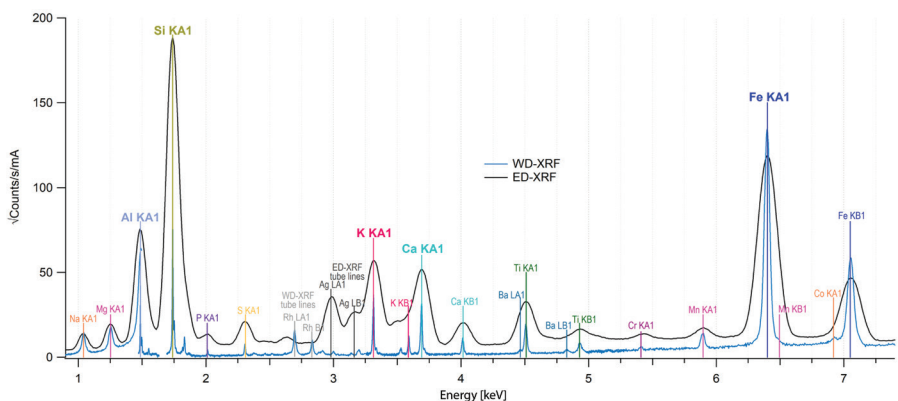


Figure 2. Fluorescence data from a cordierite sample collected with ED-XRF (black spectrum) and WD-XRF (blue spectrum). Major elements are easily identified with both methods though the increased sharpness in the WD-XRF data can help with identifying minor elements.

WD-XRF finds use in applications that require higher resolution and precision. In a WD-XRF instrument, tailored crystals are used to determine X-ray energies by reading the signal with a detector at a specific angle. Collimators can also be used to parallelize the beam and sharpen the observed peaks. The combination of crystal and collimator in the optical path are used to resolve features in the spectrum, which distinguishes WD-XRF instruments from ED-XRF.

Data collected from a sample of cordierite, a refractory silicate, via both ED-XRF and WD-XRF are shown in Figure 2. The major elements such as aluminum and silicon are easily identified with both datasets, though the WD-XRF data has higher resolution for elements such as barium, titanium, potassium, and calcium.

For a simple measurement, sample preparation is straightforward. A loose powder or liquid is poured into a cup and measured directly in air or helium through a thin polymer foil. Powders can also be pressed into stable briquets or fused into glass beads for higher precision.¹ The typical elemental range is fluorine to americium, but, with the right configuration, light elements down to carbon (using ED-XRF) and even beryllium (using WD-XRF) can be measured. XRF can cover six orders of magnitude within one measurement, starting as low as single digit parts per million.

Figure 3 shows an example of a calibration curve for magnesia in alumina using ED-XRF. The magnesium signal for measured standards is integrated and

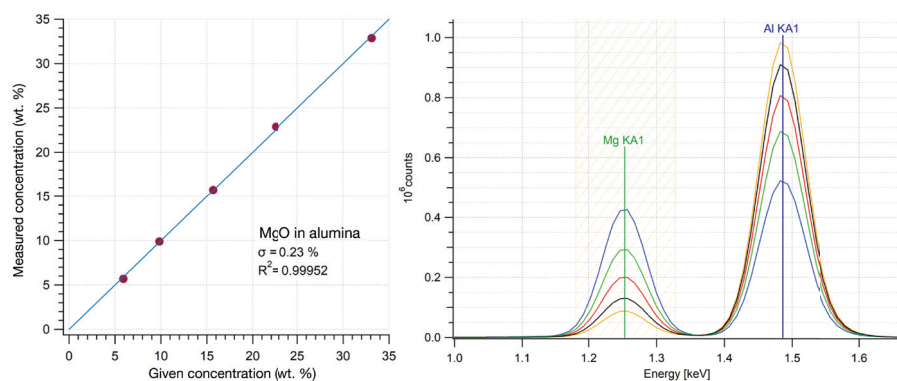


Figure 3. A calibration curve for measuring magnesia (MgO) in alumina (Al₂O₃) demonstrating a very good linearity. Plotted data is the integrated intensity for the manganese signal in the XRF spectra versus known concentration in the calibration standards. Unknowns with similar composition could be measured against this calibration curve.

plotted versus known concentration. This calibration curve can then be used for any unknown samples with the same matrix—the response for the same peak will yield the concentration in the unknown. The standard deviation shows the excellent linearity that can be achieved with an XRF measurement. This approach can also be used for calculating other parameters, such as Al/Si ratios in aluminosilicates.²

In the absence of standards, many commercially available XRF spectrometers also offer a standardless method using fundamental parameters. In this process, a model is calculated based on peak deconvolution, yielding an educated guess for sample composition.

Micro X-ray fluorescence

μXRF is an emergent technique that finds increasing use in various scientific disciplines. It excels in providing high-resolution elemental composition maps and spatial distributions, especially in the analysis of challenging samples and advanced materials.

This instrumental technique combines the principles of traditional XRF with the use of a small, focused beam of X-rays. This addition enables the measurement of elemental composition at extremely small spot sizes with excep-

tional spatial precision, down to less than 20 μm. Sophisticated polycapillary lenses help minimize the loss of X-ray intensity from traditional collimators, which in turn helps maintain high sensitivity to trace elements with detection limits as low as tens to hundreds of ppm for many elements.

A motorized stage with precise sample positioning can be used to produce elemental distribution maps and provide contextual information about areas of interest within a sample. One notable feature is the simplicity of preparing samples, making it suitable for various shapes and sizes. The collected data, presented as energy dispersive spectra for each pixel, enable a thorough examination of elemental distribution maps, providing both qualitative and quantitative insights.

Experiment design includes choice of spot size, measured intensity, and step size. These factors will determine sensitivity and spatial resolution. Further experimental conditions can include options such as various X-ray sources for optimizing specific elements of interest as well as an optional purge with helium gas, which enables the analysis of moist or wet samples. A robust standardless quantification algorithm, based on fundamental parameters, is also beneficial, particularly for the analysis of complex

materials where standards may be scarce or unavailable.

While conventional XRF finds widespread use in industrial materials such as oxides or cement, μXRF specializes in complex materials analysis, particularly where mapping and elemental distribution are pertinent. Relevant fields include materials science, microelectronics, forensics, archaeology, art conservation, and more—any application where fast elemental mapping, quantification, and trace analysis are beneficial.

An example dataset from a garnet mineral specimen is shown in Figure 4. Each pixel in the dataset has an associated ED-XRF spectrum; this information can be used to generate colored maps that correspond to distribution of identified elements. Data can be viewed not only as individual elements but also as a function of signal or concentration, allowing for multiple approaches to visualization.

X-ray diffraction

While the previously discussed techniques focus on elemental analysis, XRD is concerned with how the identified elements are connected in three-dimensional motifs. This technique provides structural information about the repeating atomic order found in crystalline materials. Relevant applications include identification of crystalline phases, distinguishing between structural polymorphs (e.g., rutile versus anatase forms of titania), quantification of mixtures, calculation of amorphous/glass content, and understanding sintering processes at elevated temperatures.

XRD studies are significant at multiple points throughout the production cycle of refractories and other ceramics: verifying phase purity of chemical precursors, testing for impurity phases or unconsumed reagents, and optimizing firing conditions for desired final products with correct physical properties.

In a traditional XRD experiment (Figure 5), a powdered sample is prepared as a flat surface and mounted in the center of the diffractometer. A goniometer provides precise control over the angular positions of the X-ray source and detector relative to the sample, down to thousandths of a degree.

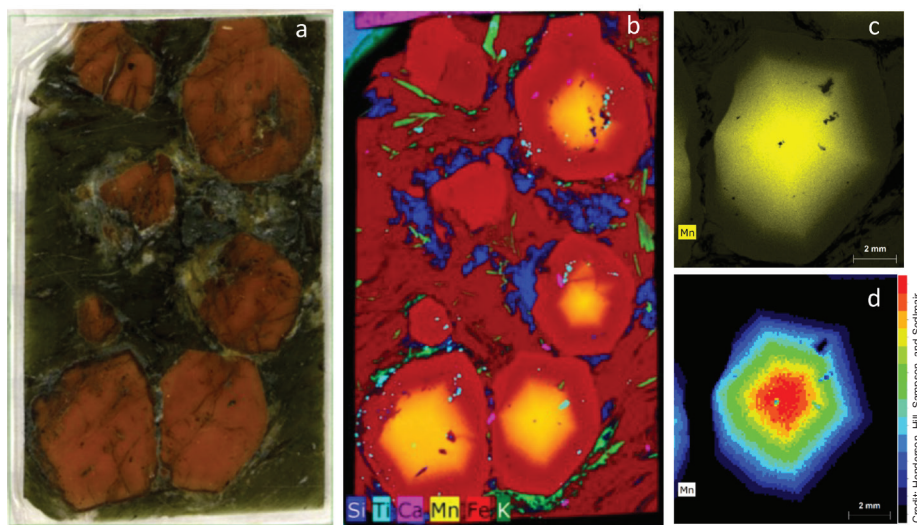


Figure 4. A thick section of a garnet sample (a) and X-ray elemental distribution map for elements silicon, titanium, calcium, manganese, iron, and potassium (b). For the bottom right crystal, an additional scan was performed using a primary filter to achieve better peak to background for the elemental peaks and minimize spectrum artifacts, such as diffraction peaks. From this measurement, the manganese distribution is displayed as intensity (c) and quantification maps (d), which show the highest intensity (highest concentration of elements) in the core of the grain.

A diffraction peak is observed as a sharp increase in signal when the Bragg equation ($n\lambda = 2d\sin\theta$) is fulfilled, which occurs at specific angles (2θ) due to constructive interference of the beam with periodic wavelength, λ . These special angles are related to characteristic distances (d) between repeating planes of atoms within a crystalline phase. The combination of peak locations and relative intensities is referred to as a diffraction pattern and can be thought of as the fingerprint for a material.

From a quantification standpoint, mixtures will exhibit convoluted signals for each phase, which can then be quantified with intensity ratios or with modeling from fundamental parameters. For the analysis of formed parts or controlled regions of interest, a spot beam can be generated with the use of specialty mirrors or collimators, though generally beam sizes for diffraction are larger (0.3–1.0 mm) than those used for μ XRF.

Quartz and cristobalite are two distinct polymorphs of silica that are found within the refractory industry. XRD data shown in Figure 6 highlight the differences between these two phases as well as that of amorphous silica glass, which does not have repeating order and thus does not demonstrate diffraction peaks.

Because many ceramic materials are synthesized in furnaces or kilns, temperature-dependent diffraction data is also helpful in understanding reaction mechanisms and formation conditions. If a diffractometer is equipped with a furnace or heater, data can be collected directly at elevated temperatures (in situ). Samples can also be characterized after sintering or processing in a stand-alone furnace (ex situ).

Some experiments involve collecting dozens or hundreds of diffraction patterns, in which case an intensity map can provide a useful way of portraying the data. The intensity map in Figure 7 shows the formation of mullite ($3\text{Al}_2\text{O}_3 \cdot 2\text{SiO}_2$) from the decomposition of kaolinite ($\text{Al}_2\text{Si}_2\text{O}_5(\text{OH})_4$) at elevated temperatures. Kaolinite converts to metakaolin around 550°C , transitions through an amorphous intermediate through 800°C , and then to $\gamma\text{-Al}_2\text{O}_3$ and mullite at $1,100^\circ\text{C}$. Higher reaction temperatures and longer durations of heating can further drive the conversion process.

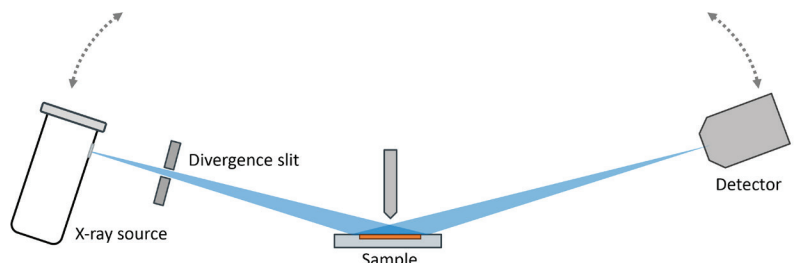


Figure 5. Schematic of a traditional Bragg diffractometer. The X-ray tube (left) and detector (right) are moved together in a coupled manner to increasingly high angles relative to the sample (center). Constructive interference will yield strong diffraction intensity at special angles that are descriptive to a crystalline phase.

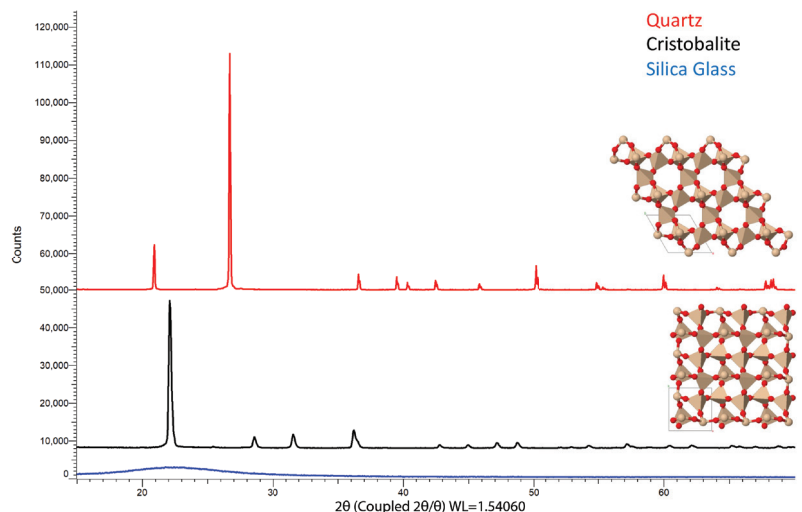


Figure 6. Diffraction data for quartz (top scan), cristobalite (middle scan), and silica glass (bottom scan). Though each polymorph is comprised of the same elements (silicon and oxygen), different arrangements of the atoms produce different fingerprint patterns. Quartz adopts a hexagonal structure (top structure), cristobalite forms a tetragonal structure (bottom structure), while silica glass has no long-range order and does not demonstrate diffraction.

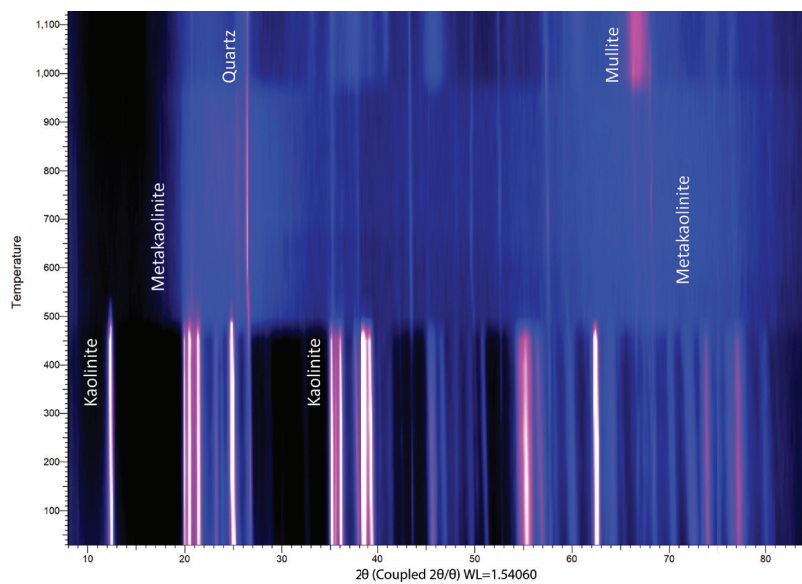


Figure 7. Intensity map for nonambient XRD data collected in situ with a heating furnace. The x-axis is 2θ , as is tradition, and the y-axis is temperature. Diffraction intensity is plotted here as a function of brightness (black is low intensity, white/pink is high intensity, blue colors are intermediate intensities).

X-ray microscopy

The final technology in this review is XRM, an imaging technique centered on two principles: contrast in X-ray transmission based on density, and geometric image magnification based on distance to a sensor. XRM is related to microcomputed tomography but extends these capabilities through the use of sophisticated software algorithms for statistical analysis and visualization as well as the potential for higher resolution.

Within the ceramics industry, XRM finds use in any application where structural imaging is desired, particularly for investigation of internal features. Samples are frequently characterized in their native state without the need for cutting, polishing, or sputter coating. Relevant uses include internal defects; void structures in porous or foamed ceramics; orientation of fibers and meshes; structural integrity of green and sintered parts formed via injection molding or 3D printing; and layer thickness in conductive oxides, such as batteries or fuel cells.

A schematic of a typical instrument is shown in Figure 8. An intense X-ray beam is generated at the source and optionally conditioned through various filters. The sample is mounted on a precision stage that allows for fine control over rotation angle; height; and distance between source, sample, and detector. As the X-ray beam passes through the sample, 2D radiographs are collected that provide information about differences in material density. Moving the sample closer to the source and further from the detector provides a magnified image from a smaller physical volume within the sample (geometric magnification).

A full experiment will collect a stack of images with variable rotation angle and height. This data can then be processed into a 3D body that will be inspected for cracks, defects, porosity, and a multitude of other physical features. Perhaps most significantly, XRM is a nondestructive technique that allows for investigations of internal structures that might not be accessible through optical or electron microscopy.

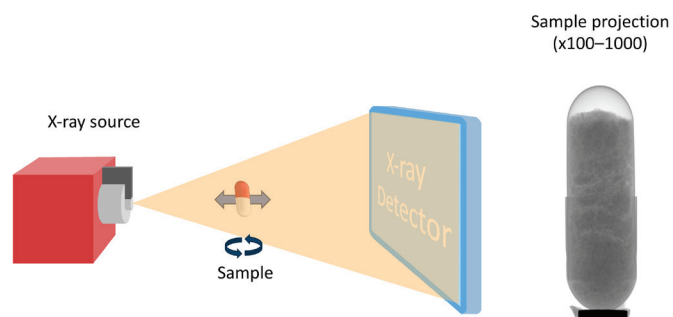


Figure 8. Schematic of an XRM experiment. The X-ray beam passes through the sample, which is placed at a specific distance from the source and detector to optimize for viewing region or magnification. The detector collects a 2D image of the sample where the beam is attenuated by more dense regions of the sample, providing contrast in the radiograph. The sample is rotated along the central axis, which provides a 3D image set that can then be reconstructed and analyzed in greater detail.

Data collected from a sandstone core are shown in Figure 9. The consolidation and structure of the silica grains is clearly seen; however, the colored images provide an additional level of clarity and visualization. In the left reconstruction, the pores are displayed as an intensity gradient based on size. Similarly, the dense mineral grains are shown on the right, again plotted as function of size. These types of studies can be furthered with statistical analysis for calculations of total pore volume, histograms of grain sizes, and more.

Case study: Injection molded ceramics

Two injection molded ceramic components were analyzed with multiple techniques to demonstrate how supporting technologies can provide a deeper level of material characterization.

The first sample—a white cylindrical fitting with a lustrous surface—was analyzed with μ XRF at multiple points along the head and body using a Bruker M4 TORNADO. Elemental analysis reveals a consistent composition across the sample with zirconium as the major identified element. Smaller amounts of yttrium, hafnium, and silicon are also identified.

Hafnium is frequently found in zirconium-containing compounds due to difficulty in separating these two elements, so its presence here is unsurprising. Yttrium and silicon content are perhaps more interesting. Pure zirconia adopts a monoclinic structure at room temperature; however, many industrial applications use tetragonal or cubic stabilized forms of zirconia that can be obtained with substitutions of cations such as Y^{3+} . The amount of dopant directly influences the stabilized form.³

Diffraction experiments provide insights into which crystalline forms are present. XRD data (Figure 10) were collected using a Bruker D8 DISCOVER diffractometer using a copper microfocus source and an EIGER2 R 500K area detector. The most intense diffraction signal is matched to the major phase, tetragonal ZrO_2 . Closer inspection of overlapping peaks reveals the presence of the cubic structure, and smaller peaks around the baseline are identified as the monoclinic form. In some specified applications, a small amount of monoclinic zirconia is

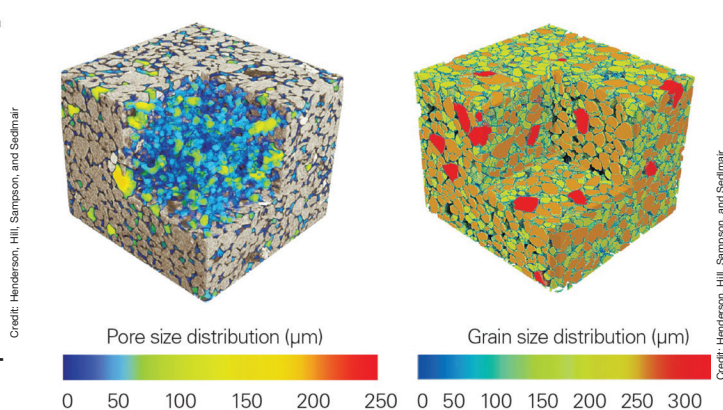


Figure 9. XRM data from a sandstone core with average size plotted as a function of intensity gradient for pores (left) and dense grains (right). This plot demonstrates a clever extension of the technique by visualizing the void space rather than the sample itself.

targeted to provide increased toughness through a stress-induced transformation. This mixture of phases is referred to as partially stabilized zirconia.

No additional peaks are observed in the diffraction data, which rules out any crystalline phases containing silicon, such as quartz or zircon. The silicon detected in the XRF data—possibly added to tailor mechanical surface behavior or optical properties, such as the refractive index⁴—is then implied to be amorphous.

A small threaded nozzle—off-white in color and with a matte finish—was characterized with joint XRD and XRM studies. The diffraction data confirm that the sample is composed of corundum (Al_2O_3 , alpha phase). A closer inspection at the peak shapes indicates much sharper peaks than the previous zirconia sample. Sharper reflections are an indication of larger crystallites within the sample, which is consistent with corundum behavior with sintering. Spotty diffraction rings (Debye rings) in the 2D data set also indicate the existence of large crystal grains.

An XRM dataset was collected with a Bruker SKYSCAN 2214 equipped with high resolution components, including tungsten filament and CMOS detector. Two primary features are observed in the image slice shown in Figure 11: a small crack on the inner wall and graininess within the sintered oxide body. The speckled appearance is not an artifact but is the result of the large grains that were observed previously in the XRD data. The internal crack is measured with maximum dimensions of $1,014 \times 126 \times 239 \mu\text{m}$ (length \times width \times depth). The diameter of the inner channel is $492 \mu\text{m}$ at the top opening and about $2,040 \mu\text{m}$ throughout the main body with some small variations. Visualization as a function of density also reveals a subtle variance between the tip of the nozzle, the wider body, and the threaded base. The tip and base are nearly identical densities and roughly 3% higher than the wider middle region.

A video of this sample reconstruction is available at www.youtube.com/watch?v=t33ewufEfSs. It demonstrates the types of visualizations possible with a fully rendered 3D dataset.

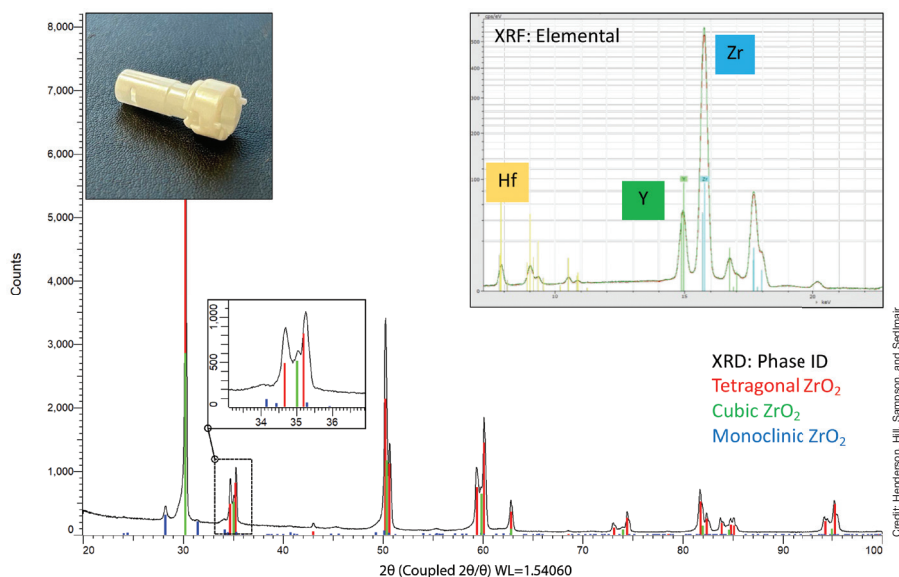


Figure 10. (insets) Elemental analysis of a ceramic fitting. Zirconium (Zr) is identified as the major element with yttrium (Y) and hafnium (Hf) also observed. The spectra from body and head overlay nicely together, indicating a similar overall composition throughout the sample. (main) Diffraction data for the zirconia sample showing the tetragonal main phase with moderate amounts of cubic and some minor/trace monoclinic phases. The stabilization into tetragonal and cubic forms is due to the substitution of yttrium for zirconium. The detection of monoclinic ZrO_2 classifies this material as partially stabilized zirconia rather than fully stabilized.

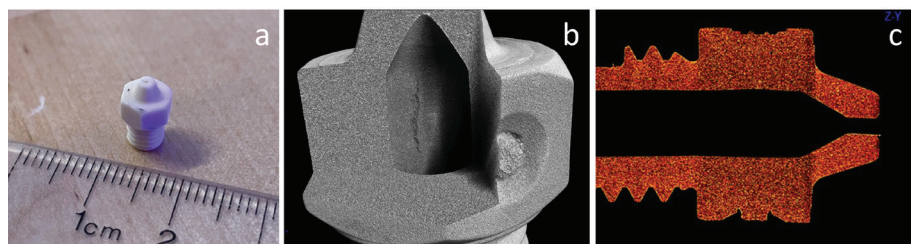


Figure 11. Selected images from an 3D XRM dataset for (a) the alumina nozzle showing (b) a small internal crack on the inner wall of the channel and (c) some observable differences in density between the end, body, and screw regions of the sample.

Concluding remarks

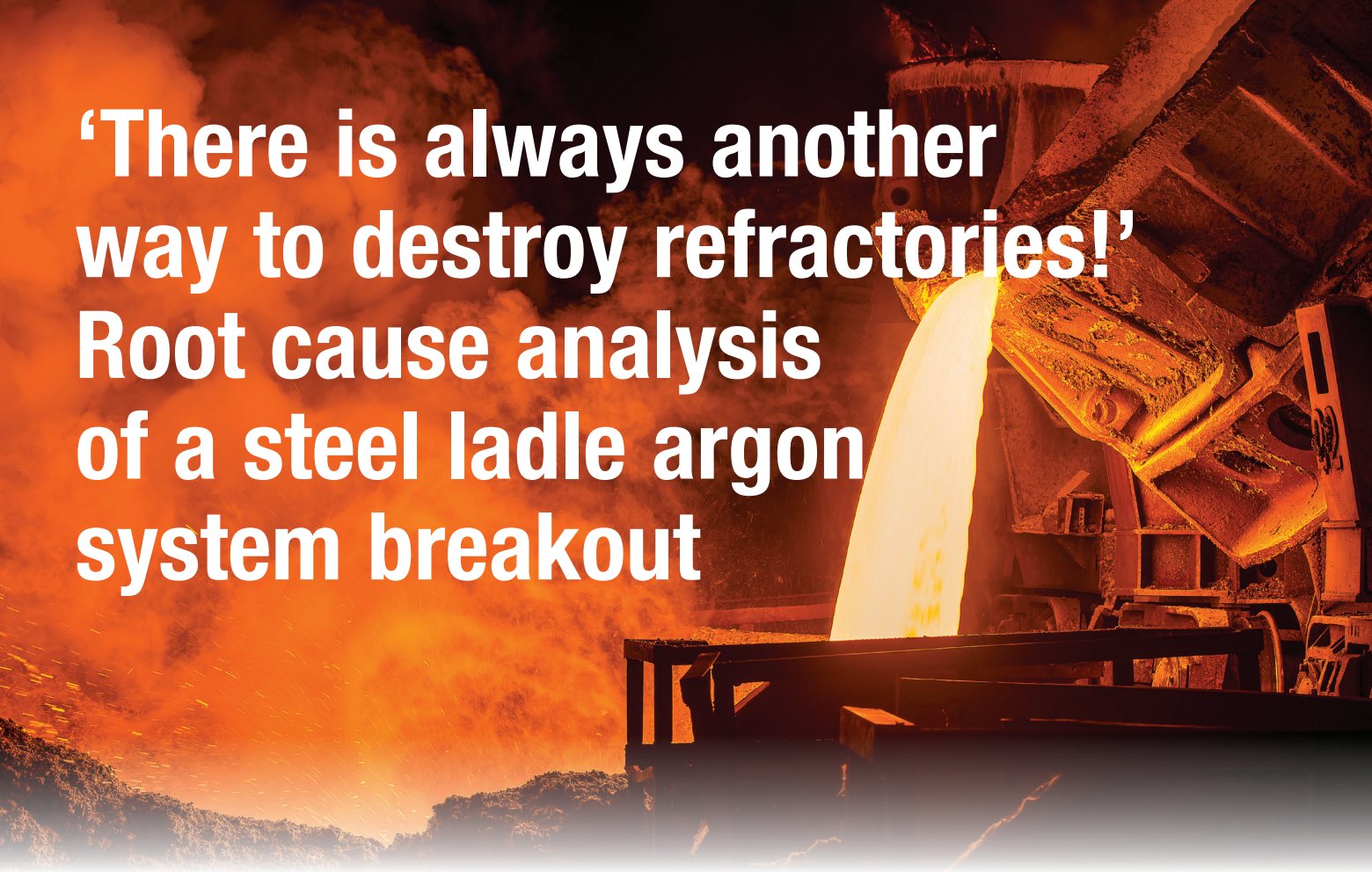
Each of the highlighted X-ray technologies reveals critically important information in materials characterization: elemental analysis with XRF and μXRF , phase analysis with XRD, and structural analysis with XRM. When used in conjunction, these analytical methods can provide a more complete understanding of a project. Additional educational videos and resources are available at www.youtube.com/bruker.

About the authors

Nathan Henderson, Tina Hill, David Sampson, and Julia Sedlmair are senior applications scientists at Bruker Corporation (Madison, Wis.). Contact Henderson at Nathan.Henderson@bruker.com.

References

- ¹Falcone, R., et al. "X-ray fluorescence analysis of raw materials for the glass and ceramic industries," *Glass Technology* 2002, **43**(1): 39–48.
- ²Georgakopoulou, Myrto, et al. "Development and calibration of a WDXRF routine applied to provenance studies on archaeological ceramics." *X-Ray Spectrometry* 2017, **46**(3): 186–199.
- ³Graeve, O.A. "Zirconia." In: Shackelford, J.F. and Doremus, R.H. (eds) *Ceramic and Glass Materials*. Springer, Boston, MA. (2008)
- ⁴Roy, M., et al. "Ceramics in bone grafts and coated implants." In: Bose, S. and Bandyopadhyay, A. (eds) *Materials for Bone Disorders*. Academic Press. (2017) ■



‘There is always another way to destroy refractories!’ Root cause analysis of a steel ladle argon system breakout

By Tom Vert

Determining the root cause of a refractory failure issue is essential for liability and safeguarding reasons. A proper root cause analysis must consider all potential sources of failure, from materials to installation to operational factors.

This article will show how root cause analysis can be used to investigate and resolve refractory failure issues, using the example of a steel ladle argon system breakout.

Breakouts are when molten metal leaks and/or pours out from the refractory-lined ladle during steel production. When breakouts occur, all personnel in a steel shop have a stake in knowing what caused the breakout to avoid future occurrences. For example, people working in operations, installation, and refractory supply will want to ensure that their practices, handiwork, and products, respectively, did not cause the breakout, and if they did, what changes need to be made to error-proof the system.

Determining the cause(s) of a breakout can help personnel and companies avoid liability. With so many stakeholders, diplomatic skills are a must for someone conducting a break-

out investigation. But even if everyone performed their job perfectly, breakouts will inevitably occur at some point during production due to the wide range of possible failure modes. So, identifying the root cause(s) behind a breakout will allow personnel to put measures in place to avoid future failures.

This article describes the fundamentals to conducting a proper root cause analysis. Such an analysis will give all personnel confidence in the results and drive the prevention phase of the investigation.

Background: The mechanics of a steel ladle argon system breakout

When molten steel is placed in a refractory-lined ladle to undergo refinement before casting, stirring the molten mixture is necessary to ensure optimal control of temperature and chemistry during critical grade manufacturing. But depending on the stir system used, there is a risk that the molten mixture will breakout from the ladle.

There are two main stir systems commercially available: indirect stirring (through electromagnetic forces) and direct stirring (through refractory argon plugs). While the former option does not come with the risk of molten steel breakout, the latter option is more common because it allows for much more vigorous and controllable stirring, as well as avoiding the major capital cost of installing an electromagnetic system.

In a direct stirring system (Figure 1), argon is injected through a piping system into the bottom of the steel ladle. The argon plugs are made of a permeable refractory that allows the gas to flow at the rate necessary for good stirring. Over time,

the plugs will wear down and must be replaced with new ones, typically after 10–20 uses. Sometimes, the wear is accelerated and/or the plugs are not replaced at the right moment. In that case, the 20–350 tons of molten steel may break out from the ladle and escape, resulting in damages to major equipment (Figure 2).

To determine the root cause(s) of a molten steel breakout, the first step is to ensure all refractories are preserved before demolition so that a thorough analysis can be conducted. Ruling out potential failure modes can be just as useful as identifying the right one because direct observation of certain breakout pathways is not always available. For example, molten steel can flow out of the ladle with such force that the argon plug itself and/or the sleeve is washed out, so they are not available for review.

Figure 3 shows the seven main failure modes through which molten steel escapes the ladle during a breakout event. Failure modes 1, 2, and 3 usually can be determined by the physical evidence of deteriorated refractories and/or steel skulls left over from the breakout. In contrast, failure modes 4, 5, 6, and 7 can be harder to find, and so require a review of the following key evidence:

- Last laser and/or visual analysis of the hot face of the ladle argon plug at the lay down stand.
- Information on oxygen lancing history (e.g., frequency, pressures, times).
- Stirring history of the plugs (e.g., # of heats, length of stirring, long stirring, flow rates, pressures).
- Installation history of the plugs (e.g., who changed them, installation practices, proximity to the failure).

There are 57 factors that are recognized as potential root causes for breakout failures, classified generally as material failures, installation practices, and operating/processing practices, and usually, some combination of these. An investigator must be open minded and review every potential failure to determine what is the root cause and then find a way to eliminate it.

The seven failure modes of molten steel breakout

During root cause analysis, an investigator will consider each of the following failure modes and determine which mode, or more accurately, which combination of modes led to the breakout of molten steel.

Mode 1: Failure of block support

Failure cause: The supporting refractory material around the block either wears too quickly, cracks, and/or spalls, creating an easy pathway through which molten steel can flow. The steel may take a few heat cycles to break through due to freezing near the ladle shell, but if true integrity is lost, then it will make its way down, creep under and/or lift the block, and break out.

Potential refractory cause(s)

- Failure of the refractory material due to poor quality from the supplier.
- Failure of refractory material due to over aged and/or improper storage (e.g., stored in high humidity area).

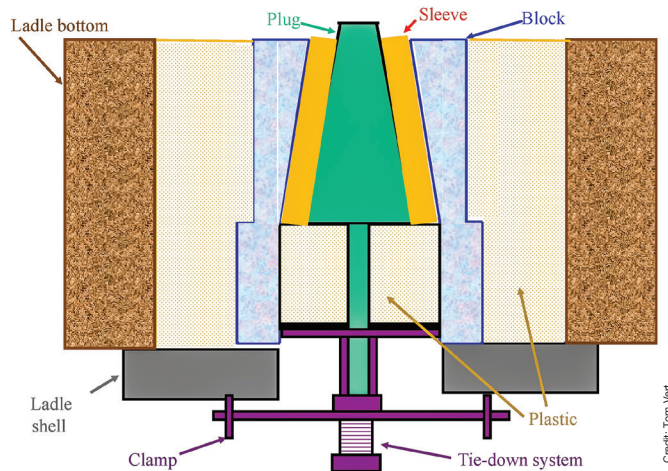


Figure 1. Typical argon stirring system layout.

- Low quality material chosen for an application with higher slag and/or temperature resistance.

Potential installation cause(s)

- Ram or plastic not installed dense enough and/or with air pockets due to poor ramming equipment and/or technique.
- Castable not installed and/or dried out properly with too much water and/or poor material or ambient temperature control, leading to poor density and/or minimal bonding strength.

Potential process cause(s)

- Surrounding material damaged due to improper dig out on block and/or plug changes.
- Extremely aggressive slags eating into the surrounding material and causing extreme unexpected wear.
- Extreme oxygen lancing in the wrong spot eating into the surrounding material and causing extreme unexpected wear.

Mode 2: Failure of refractory block (assuming a precast block is used)

Failure cause: The main refractory block either wears too quickly, cracks, and/or spalls, creating an easy pathway through which molten steel can flow. The steel may take a few heat cycles to break through due to freezing near the ladle

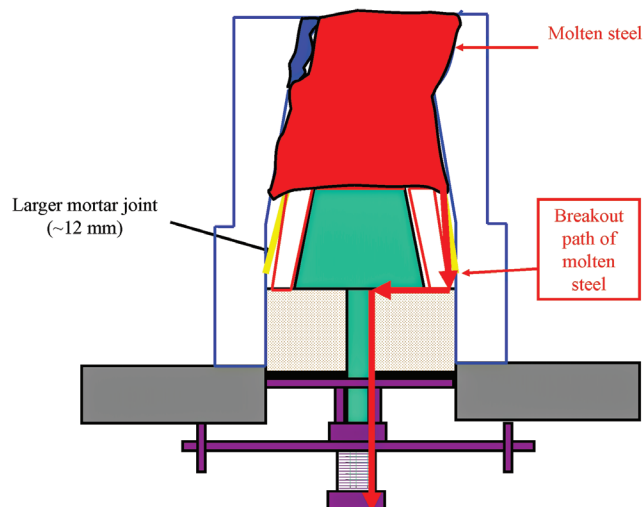


Figure 2. An illustration showing one pathway that molten steel can take during a breakout event.

'There is always another way to destroy refractories!' Root cause analysis of a . . .

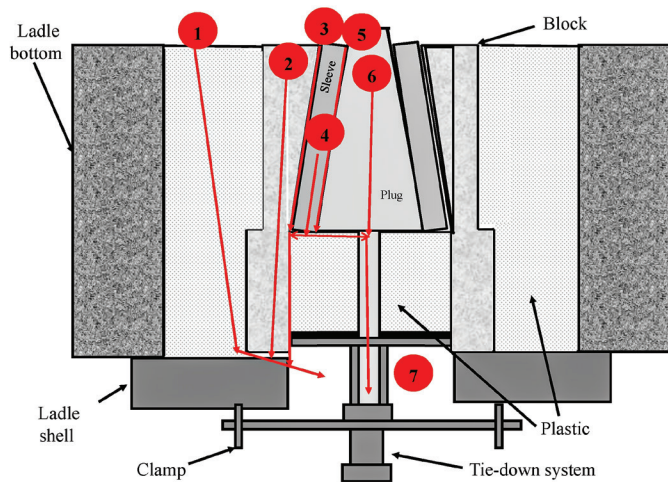


Figure 3. Seven main failure modes through which molten steel escapes in a direct stirring system: 1) plastic refractory joint, 2) refractory surround block, 3) joint between block and sleeve, 4) sleeve itself (and supporting plastic), 5) joint between the sleeve and plug, 6) argon plug itself (and supporting plastic), and 7) argon plug itself and piping system.

shell, but if true integrity is lost, then it will make its way down and break out.

Potential refractory cause(s)

- a. Failure of refractory material due to poor quality from supplier.
- b. Failure of refractory material due to over aged and/or improper storage (e.g., getting soaked in water in storage).
- c. Low quality material chosen for an application with higher slag and/or temperature resistance.
- d. Improper refractory shape (i.e., square blocks always crack in service).

Potential installation cause(s)

- e. Block is not installed level and secure leading to stress and then cracks.
- f. Supporting refractory is not installed and/or dried out properly with too much water and/or poor material or ambient temperature control, leading to poor density and/or minimal bonding strength and then a moving and/or cracking block (see Mode 1 for more info).

Potential process cause(s)

- g. Block is damaged due to improper dig out on block and/or plug changes.
- h. Extremely aggressive slags eating into the block and causing extreme unexpected wear.
- i. Extreme oxygen lancing in the wrong spot eating into the block material and causing extreme unexpected wear.

Mode 3: Failure of joint between block and sleeve

Failure cause: The joint between the main refractory block and the sleeve joint becomes compromised, creating an easy pathway through which molten steel can flow. The steel may take as little as one heat cycle to break through, at which point it will make its way down through the natural path and break out.

Potential refractory cause(s)

- a. Failure of refractory material due to poor quality from supplier.
- b. Failure of refractory material mortar due to improper mixing and/or over aged and/or improper storage (e.g., getting frozen).
- c. Low quality material chosen for an application with higher slag and/or mechanical strength requirement.

Potential installation cause(s)

- d. Sleeve is not installed properly due to bad mortaring (too much mortar and too thick a joint), leading to a loose installation and potential cracking and/or joint and/or sleeve movement.
- e. Sleeve is not installed properly due to bad mortaring (too little mortar and too thin a joint), leading to a tight installation and potential cracking/stress and/or joint.

Potential process cause(s)

- f. Block is damaged and/or worn low (high wear and/or run too long), leading to direct access to the lower joint area.
- g. Improper cleanout of slag/steel at hot face of plug/sleeve/block, leading to sleeve not sitting in correct location and open and/or offset joint (note that this condition can lead to Mode 3d failure, large joint).

Mode 4: Failure of refractory sleeve (assuming precast sleeve is used)

Failure cause: The main refractory sleeve either wears too quickly, cracks, and/or spalls, creating an easy pathway through which molten steel can flow. The steel may take a few heat cycles to break through due to freezing near the ladle shell, but if true integrity is lost, then it will make its way down and break out.

Potential refractory cause(s)

- a. Failure of refractory material due to poor quality from supplier.
- b. Failure of refractory material due to over aged and/or improper storage (e.g., getting soaked in water in storage).
- c. Low quality material chosen for an application with higher slag and/or temperature resistance.
- d. Improper refractory shape (i.e., too thin a sleeve [< 30 mm] can lead to cracks in service).

Potential installation cause(s)

- e. Sleeve is not installed level and secure, leading to stress and then cracks.
- f. Supporting refractory is not installed and/or dried out properly with too much water and/or poor material or ambient temperature control, leading to a moving and/or cracking sleeve (see Mode 3 for more info).

Potential process cause(s)

- g. Sleeve is damaged due to improper dig out on plug changes.
- h. Extremely aggressive slags eating into the sleeve causing extreme unexpected wear.
- i. Extreme oxygen lancing in the wrong spot eating into the sleeve material and causing extreme unexpected wear.

Mode 5: Failure of joint between sleeve and plug (for systems with a sleeve)

Failure cause: The joint between the main refractory sleeve and the plug joint becomes compromised, creating an easy pathway through which molten steel can flow. The steel may take as little as one heat cycle to break through, at which point it will make its way down through the natural path and break out.

Potential refractory cause(s)

- a. Failure of refractory material due to poor quality from supplier.
- b. Failure of refractory material mortar due to improper mixing and/or over aged and/or improper storage (e.g., getting frozen).
- c. Low quality material chosen for an application with higher slag and/or mechanical strength requirement.

Potential installation cause(s)

- d. Plug is not installed properly due to bad mortaring (too much mortar and too thick a joint), leading to a loose installation and potential cracking and/or joint and/or plug movement.
- e. Plug is not installed properly due to bad mortaring (too little mortar and too thin a joint), leading to a tight installation and potential cracking/stress and/or joint opening.

Potential process cause(s)

- f. Sleeve is damaged and/or worn low (high wear and/or used too long), leading to direct access to the lower joint area.
- g. Improper cleanout of slag/steel at hot face of plug/sleeve, leading to plug not sitting in correct location and open and/of offset joint (note that this condition can lead to Mode 5d failure, large joint).

Mode 6: Failure of refractory plug

Failure cause: The main refractory plug either wears too quickly, cracks, and/or spalls, creating an easy pathway through which liquid steel can flow. The steel may take a few heat cycles to break through due to freezing near the ladle shell, but if true integrity is lost, then it will make its way down and break out.

Potential refractory cause(s)

- a. Failure of refractory material due to poor quality from supplier.
- b. Failure of refractory material due to over aged and/or improper storage (e.g., getting magnesia plug soaked in water).
- c. Low quality material chosen for an application with higher slag and/or temperature resistance (e.g., low alumina plug for low price).
- d. Improper refractory type (i.e., porous vs slit vs combination plug).
- e. No argon plug wear indicator (either shape and/or radiant color), making it hard to read.

Potential installation cause(s)

- f. Argon plug is not installed level and secure, leading to stress and then cracks.

- g. Supporting refractory joint is not installed properly, leading to a moving and/or cracking plug (see Mode 5 for more info).

Potential process cause(s)

- h. Plug is damaged due to improper dig out on the plug change, in either plug or sleeve area.
- i. Extremely aggressive slags eating into the plug and causing extreme unexpected wear.
- j. Extreme oxygen lancing in the wrong spot eating into the plug material and causing extreme unexpected wear.
- k. Thick slag and/or steel layer covering plug, making it hard to read.
- l. Oxygen contaminates the argon system and burns the plug out from back side internally.

Mode 7: Failure of argon plug support system

Failure cause: The mechanical support system located behind the plug (including the refractory plastic) becomes loose, leading to plug and/or sleeve movement, including joint openings, that creates an easy pathway through which molten steel can flow. The steel may take a few heat cycles to break through due to freezing near the ladle shell, but if true integrity is lost, then it will make its way down and break out.

Potential refractory cause(s)

- a. Failure of refractory material due to poor quality from supplier.
- b. Failure of refractory material due to over aged and/or improper storage (e.g., getting soaked in water).

Potential installation cause(s)

- c. Supporting refractory is not installed and compacted enough, leading to loss of density and looseness in the system.
- d. Supporting mechanical system is not installed and/or secured properly leading to movement of supporting plastic and/or plug/sleeve moving and/or cracking with path for steel to follow. (Note that head pressure of entire heat can quickly pressurize any looseness and the heat will be lost).

Potential process cause(s)

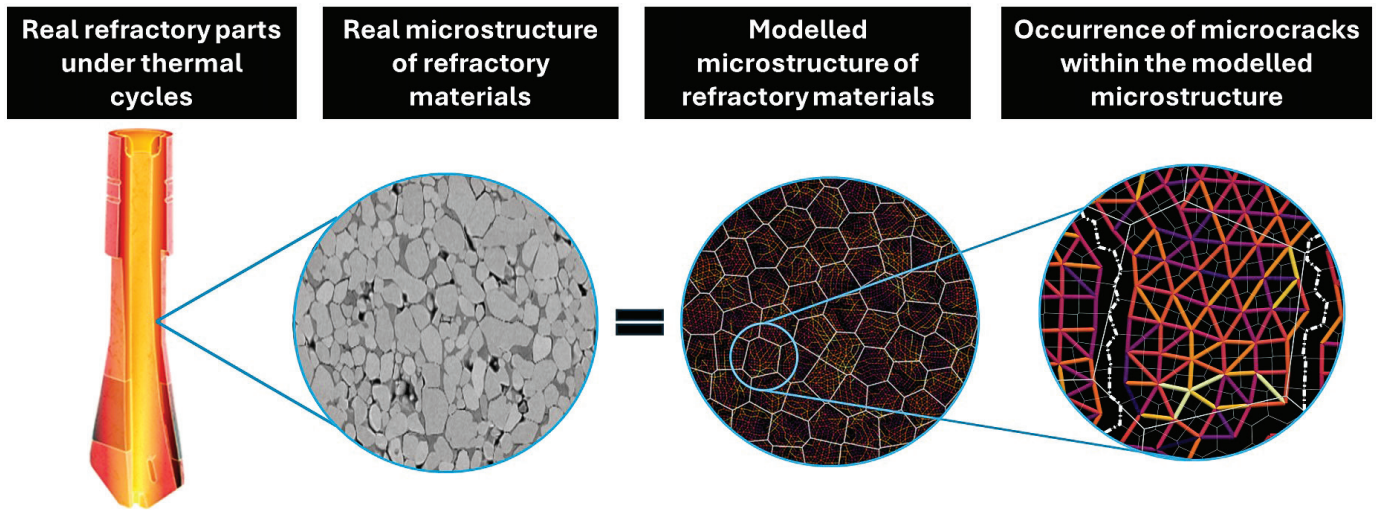
- e. Mechanical system or argon hoses are ripped off /damaged/bent, leading to loss of supporting mechanical system.

Conclusions

Root cause analysis of a steel ladle argon system breakout is an exhaustive process that incorporates a detailed review of all relevant material, installation, and/or processing anomalies that result in loss of the molten steel. An open mind, a detailed process, and a determination not to be swayed by theory but only by facts are all required if the root cause is to be found. Only in this way can a proper engineering solution be tailored to mitigate the possibility of future breakout events.

About the author

Tom Vert is an independent consultant through his company Strategic Refractory Consulting (Hamilton, Canada). Contact Vert at tomvert90@gmail.com. ■



Schematic diagram showing the link between real microstructures and discrete element modeling. Images reproduced with permission from Reference 1 and www.vesuvius.com. Descriptive captions provided by Damien André.

Credit: Moully et al., Journal of the American Ceramic Society, www.vesuvius.com

Discrete element modeling deepens understanding of microcracking phenomena in refractory materials

By Harikeshava Ranganathan, Damien André, Marc Huger, Ratana Soth, and Christoph Wöhrmeyer

A new discrete element method provides a deeper understanding of the relationship between a refractory’s microstructure and its macroscopic thermomechanical properties—paving the way to use microcrack engineering for commercial refractory production.

Though defects are often associated with weakening mechanical properties, the purposeful introduction of microcracks into refractory materials can improve their thermal shock resistance.

Refractories are heterogeneous materials, consisting of numerous aggregates within a brittle matrix.^{1,2} Microcracking occurs during synthesis when the refractory is cooled from its sintering temperature due to the heterogeneity and anisotropy of thermal expansion coefficients of each constituent.^{3,4} The presence of numerous microcracks within the microstructure can promote a significant nonlinear macroscopic mechanical response, which improves the material’s resistance to thermal shock.^{1,3,4}

Improved thermal shock resistance is a desirable property for refractories in steel making, cement making, glass processing, and other high-temperature industries. However, the relationship between a refractory’s microstructure and its macroscopic thermomechanical properties is complex, and deeper understanding of this relationship is needed to enable the use of microcrack engineering for commercial production.

As part of the European Union-funded CESAREF project (www.cesaref.eu), the authors developed a novel discrete element method (DEM) to deepen understanding of the refractory microstructure–property relationship. The development, testing, and prospects for this tool are described in the following sections.

Background: Numerical methods for modeling the refractory microstructure–property relationship

Numerical modeling is a vast field with different numerical approaches. Many researchers have used the finite element method (FEM), which breaks down complex systems into smaller elements for analysis, to comprehend the mechanics of bulk materials for high-temperature applications.⁵ However, FEM’s limitations include its computational time-consuming nature due to dynamic meshing and its difficulty in analyzing fractures without considering preexisting crack location, path, and growth at the microstructure level.

The extended finite element method (XFEM) was introduced as an improvement on FEM due to its ability to describe

discontinuities without mesh refining.⁶ However, this approach, unlike FEM, does not allow researchers to capture nucleation of multiple microcracks. Additionally, it is difficult to depict the opening and closing of microcracks at the microstructure level.

Phase-field modeling (PFM) was introduced as another method to investigate multiple crack nucleation, propagation, and branching behaviors at the microstructure level. While PFM shares some similar concepts with FEM, it relies on different criterion for the simulation. For this reason, PFM can accurately replicate crack morphology of experimental tests, but model discrepancies may lead to unrealistic crack growth in simulations due to difficulties in capturing the complete microstructure characteristics.⁷

These limitations with the above continuum approaches led researchers to start using DEM for refractory applications. Initially, DEM was used to investigate the free flow of granular particles from a silo or hopper.⁸ Later, DEM was adopted for performing thermomechanical simulations on a cohesive medium.^{8,9} Today, DEM is seen as an advanced numerical technique that can be used to perform multiphysics, multiscale, and quasi-brittle analysis for cohesive mediums.^{2,10,11}

Unlike FEM, XFEM, and PFM, which represent systems as a single continuum, DEM represents bodies as discrete particles. These particles interact with their neighbors according to contact interaction laws,^{8,9} which state that microscale interactions result in emergent properties that can be measured on the macroscale as an apparent property.¹¹⁻¹³ As such, DEM offers significant potential for modeling microstructures with numerous discontinuities, such as inclusions, cracks, debonding, and porosity, as seen in many refractory microstructures.

Previously, researchers used DEM with contact models between spherical discrete elements for investigating the relationship between the refractory microstructure and the macroscopic thermomechanical properties.¹⁴⁻¹⁶ The current study instead uses polyhedral discrete elements, as described in

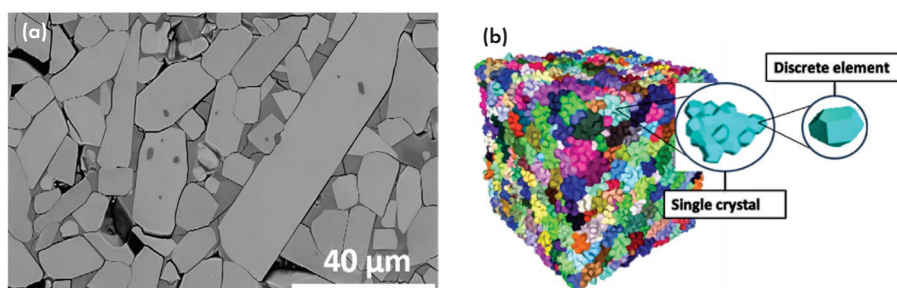


Figure 1. The real microstructure (a) and DEM model (b) of aluminum titanate, which was used as the reference material in this study.

Reference 14, to investigate this relationship. Similar to Reference 14, the phases in the model are assumed to be chemically inert, and the presences of interphases are negligible in the model microstructure.

Numerical procedure

Reference model material: Polycrystalline aluminum titanate

Polycrystalline aluminum titanate (Figure 1a) was chosen as the reference material because the numerous microcracks within its microstructure lead to a very low thermal expansion and high thermal shock resistance.¹

These microcracks result from high anisotropic thermal expansion coefficients of the individual grains, which generate internal stresses within the microstructure during the cooling stage right after sintering.^{1,4} The resulting microcracked microstructure, after complete cooling, promotes a significant quasi-brittle behavior in tension.

The DEM model aimed to qualitatively reproduce this tensile behavior (microcracks nucleation and their influences on the macroscopic mechanical properties), which is typical in many industrial refractory materials.¹ The simulation is performed with GranOO (www.granoo.org), an opensource discrete element workbench. The input data used in this DEM simulation, which represent local properties of each aluminum titanate grain at 1,200°C, are summarized in Table 1.

The DEM numerical sample is a box with dimensions of 100 μm × 100 μm × 100 μm to mimic the bulk cohesive medium. Each crystal in the numerical sample is assigned a random orientation, which is depicted by the crystal having different colors (Figure 1b), and they are built by assembling about 40 polyhedral discrete elements of random sizes. The polyhedral discrete elements are assigned the physical, mechanical, and thermal properties given in Table 1. The model is imposed with the elastic brittle law and local failure criteria.

Table 1. Input data used in the DEM simulation, assumed to be representative of local properties of each aluminum titanate grain at 1,200°C.¹

*Experimental parameters used in the simulation. **Numerical parameters used in the simulation.

| Parameter | Notation | Value | Unit |
|--|---------------|-------------------------|-----------------|
| Young's modulus* | E | 170 | MPa |
| Poisson's ratio* | ν | 0.28 | – |
| Coefficient of thermal expansion along \vec{a} * | α_a | -1.975×10^{-6} | K ⁻¹ |
| Coefficient of thermal expansion along \vec{b} * | α_b | 9.9351×10^{-6} | K ⁻¹ |
| Coefficient of thermal expansion along \vec{c} * | α_c | 17.264×10^{-6} | K ⁻¹ |
| Maximum tensile strength** | σ_t | 350 | MPa |
| Maximum compressive strength** | σ_{ic} | 3500 | MPa |
| Number of crystals** | N | 500 | – |
| Number of DE** | N_{DE} | ≈20k | – |

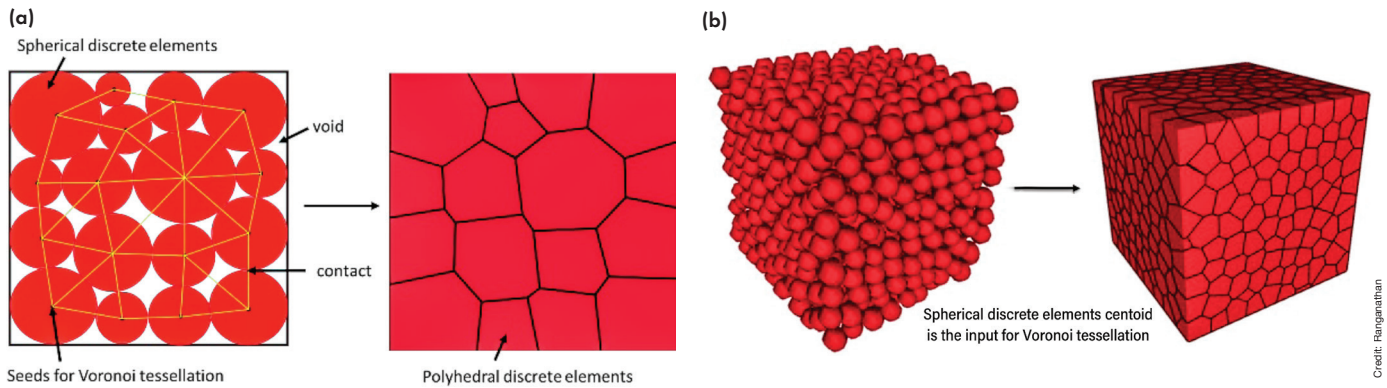


Figure 2. The Voronoi tessellation process: a) 2D sketch and b) 3D view with discrete elements.

Lattice spring model and Voronoi tessellation

The DEM introduces discrete element interactions into the simulation through so-called contact models. In literature, many contact models exist: dual spring model,¹⁶ flat-joint,¹² and cohesive beam,¹³ to name a few. Among them, the lattice spring model (LSM) is an advanced contact model because of its ability to deal directly with continuous mechanical properties, such as stress and strain. In this aspect, fastidious calibration steps can be avoided with LSM, and material thermomechanical properties, such as Young's modulus (E), Poisson's ratio (ν), and coefficient of thermal expansion (α), can be directly introduced in the model.

However, this introduction is possible only if the interaction surfaces between the discrete elements are equivalent to a continuum medium without voids. So, to obtain a domain equivalent to a continuum medium, a plane-sweeping algorithm called a Voronoi tessellation is processed on the dedicated domain.

In a Voronoi tessellation, several points scattered on a plane are subdivided into exactly n cells that enclose a portion of the plane closest to each point. To generate scattered points for the tessellation, transitory spherical discrete elements (in a predefined range of size) are filled in the domain, as shown in Figure 2a. The centroids of the transitory spherical discrete elements are used as input for the Voronoi tessellation to generate polyhedral elements. These polyhedral discrete elements are connected using contacts (yellow line in Figure 2a) generated by a Delaunay tessellation. So, the process to generate the DEM model (with LSM) involves dual tessellation. For more details about the fundamental aspects of the LSM contact model, readers can refer to Reference 9.

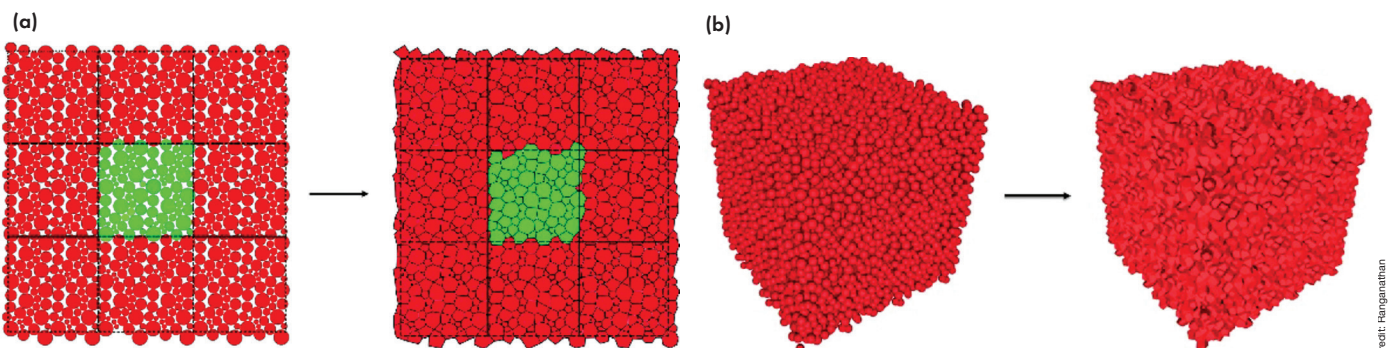
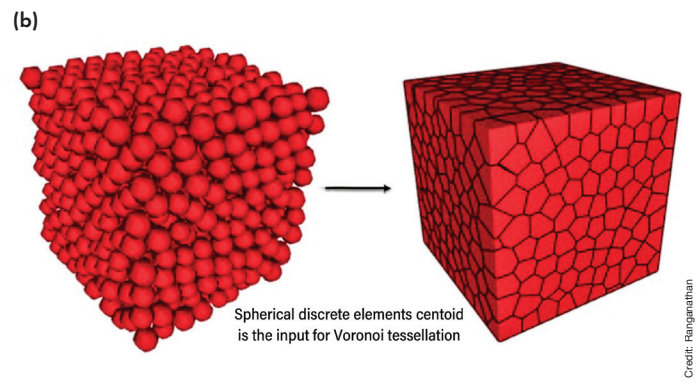


Figure 3. Voronoi tessellation process for periodic boundary conditions: a) 2D sketch and b) 3D view with discrete elements.

Thermomechanical simulations

The thermomechanical simulation is segregated into two steps. The first step is the cooling process, where the sample is cooled down from 1,200°C to 900°C. During this cooling step, some microcracks are initiated and propagated due to the anisotropic thermal expansion of the crystals. After the cooling stage, the numerical sample with microcracks is obtained. The second step is to perform a uniaxial tensile test on the obtained numerical sample to monitor the macroscopic materials' mechanical response in terms of strain versus stress evolution (Figure 5).

Discussion

As seen in Figure 5, the microcracked numerical sample exhibits a significant nonlinear mechanical response under tension when cooled from 1,200°C to 900°C. When cooled even further, to 600°C (Figure 6a), the sample shows a similar nonlinear mechanical response under tension. On the other hand, in the case of the numerical sample with no microcrack, it exhibits a brittle mechanical response under tensile test (see the 1,200°C curve in Figure 6a).

This difference in the mechanical response supports the claim that the microcracks network strongly influences the thermomechanical properties of the (aluminum titanate) refractory materials. Additionally, the stress–strain curves depict a strong variation from brittle fracture to quasi-brittle behavior depending on the number of preexistent microcracks.¹

Similar mechanical responses were observed when microcracked aluminum titanate samples that were cooled down from 1,400°C to 850°C and 20°C were then loaded under tensile test (Figure 6b). The microstructure with no microcracks exhibited a brittle response (Figure 6b at 850°C) and the microstructure with a huge microcracks network exhibited a large nonlinear mechanical response (Figure 6b at 20°C).

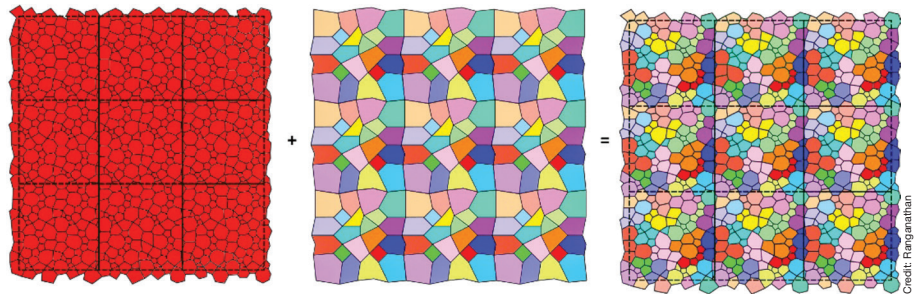


Figure 4. 2D sketch of the numerical polycrystalline representative volume element (RVE), accounting for periodic boundary conditions obtained by Voronoi tessellation.

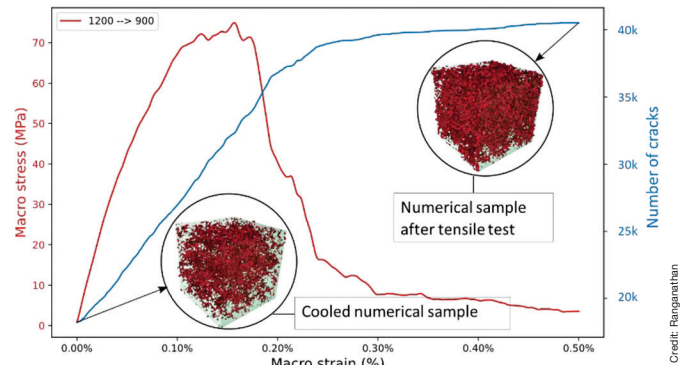


Figure 5. Mechanical response of the numerical sample under uniaxial tensile stress.

Conclusion and future directions

To clarify the relationship between microstructure and macroscopic properties in refractory materials, a DEM model was developed and tested using aluminum titanate as a reference. This simulation successfully captured the microcracking phenomena during cooling and then during tensile loading, as well as the macroscopic stress–strain law, demonstrating the potential of DEM models to deepen understanding of the refractory microstructure–property relationship.

In the future, this novel tool could be used to help visualize the evolution of Young's modulus, Poisson's ratio, and the coefficient of thermal expansion of aluminum titanate materi-

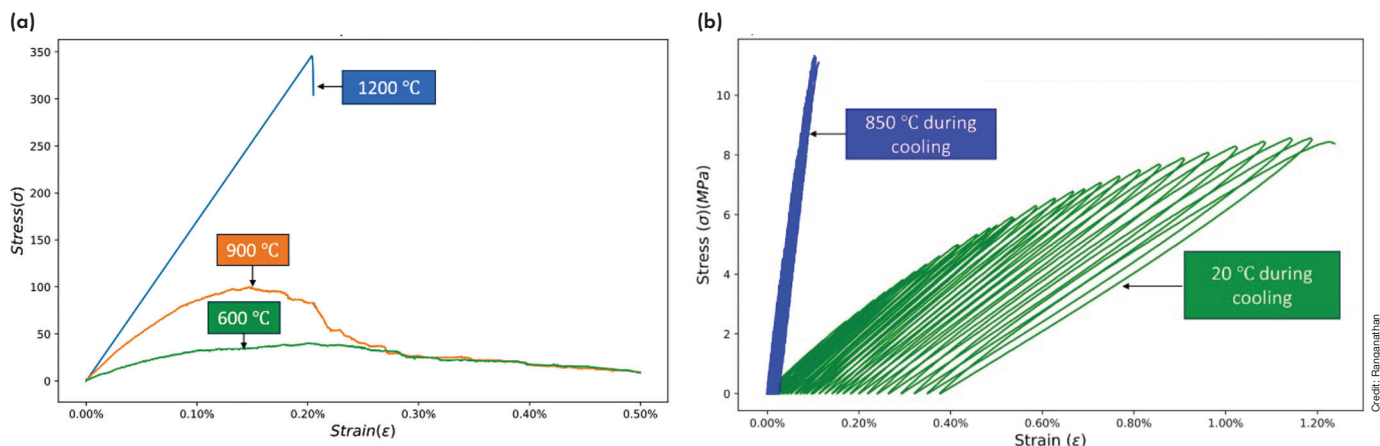


Figure 6. Evolution of the nonlinearity in the stress–strain curve in tension on polycrystalline aluminum titanate materials at different temperatures after a given cooling stage. a) DEM simulation results at 1,200°C, 900°C, and 600°C (after cooling from 1,200°C). b) Experimental results at 850°C and 20°C (after cooling from 1,400°C).

Discrete element modeling deepens understanding of microcracking phenomena . . .

als versus temperature. First, however, the GranOO platform used in this study should be upgraded so it can capture phenomena such as crack healing mechanisms and crack trajectory mapping. These new data will help the refractory industry to improve on the design of their materials.

About the authors

Ratana Soth and Christoph Wöhrmeyer are scientist and refractory team lead, respectively, at Imerys Technology Center (Vaulx-Milieu, France). Harikeshava Ranganathan, Damien André, and Marc Huger are Ph.D. student, research associate, and professor, respectively at the University of Limoges, France. Contact Ranganathan, André, or Huger at harikeshava.ranganathan@unilim.fr, damien.andre@unilim.fr, or marc.huger@unilim.fr.

References

- ¹M. Mouiya et al., “The stress–strain behavior of refractory microcracked aluminum titanate: The effect of zigzag microcracks and its modeling,” *Journal of the American Ceramic Society*, vol. 106, 2023, pp. 6995–7008.
- ²W. Du et al., “Discrete element modeling of ordinary refractory ceramics under cold crushing testing: Influence of minimum element size,” *Ceramics International*, vol. 48, 2022, pp. 17934–17941.
- ³R. G. Bourdel et al., “Influence of thermal damage occurrence at microstructural scale on the thermomechanical behavior of magnesia–spinel refractories,” *Journal of the European Ceramic Society*, vol. 32, 2012, pp. 989–999.
- ⁴M. G. Kakroudi et al., “Anisotropic behavior of andalusite particles used as aggregates on refractory castables,” *Journal of the European Ceramic Society*, vol. 29, 2008, pp. 571–579.
- ⁵M. Kuna, “FE techniques for crack analysis in elastic-plastic structures,” *Finite Elements in Fracture Mechanics: Theory-Numerics-Applications*, vol. 201. 2013, pp. 305-325.
- ⁶Y. Wang et al., “From diffuse damage to sharp cohesive cracks: A coupled XFEM framework for failure analysis of quasi-brittle materials”, *Computer Methods in Applied Mechanics and Engineering*, vol. 299, 2016, pp. 57–89.
- ⁷T. T. Nguyen et al., “Initiation and propagation of complex 3D networks of cracks in heterogeneous quasi-brittle materials: Direct comparison between in situ testing-microCT experiments and phase field simulations,” *Journal of the Mechanics and Physics of Solids*, vol. 95, 2016, pp. 320–350.
- ⁸M. H. Moreira et al., “Discrete element modeling—A promising method for refractory microstructure design,” *American Ceramic Society Bulletin*, vol. 99, 2020, pp. 22–28.
- ⁹D. André et al., “A novel DEM approach for modeling brittle elastic media based on distinct lattice spring model,” *Computer Methods in Applied Mechanics and Engineering*, vol. 350, 2019, pp. 100–122.
- ¹⁰A. S. Grigoriev et al., “Analysis of the quasi-static and dynamic fracture of the silica refractory using the mesoscale discrete element modeling,” *Materials*, vol. 14, 2021, p. 7376.
- ¹¹D. André et al., “Discrete element method to simulate continuous material by using the cohesive beam model,” *Computer methods in applied mechanics and engineering*, vol. 213–216, 2012, pp. 113–125.
- ¹²F. ASADI, “Micro-mechanical modeling of heterogeneous materials containing microcracks with discrete element method (DEM),” PhD, IRCER, Limoges, 2021.
- ¹³T. Thi. Nguyen, “Numerical modeling of microstructure–properties relationships of refractories: micro-mechanical approach with the discrete element method. Diss. Limoges,” Thesis, IRCER, Limoges, 2019.
- ¹⁴D. André et al., “A discrete element thermo-mechanical modeling of diffuse damage induced by thermal expansion mismatch of two-phase materials,” *Computer Methods in Applied Mechanics and Engineering*, vol. 318, 2017, pp. 898–916.
- ¹⁵S. Nosewicz et al., “Discrete element framework for determination of sintering and post sintering residual stresses of particle reinforced composites,” *Materials*, vol. 13, 2020, p. 4015.
- ¹⁶P. R. Prakash et al., “A meso-scale discrete element method framework to simulate thermo-mechanical failure of concrete subjected to elevated temperatures,” *Engineering Fracture Mechanics*, vol. 239, 2020, p. 107269. ■

10TH INTERNATIONAL
CONGRESS ON
CERAMICS
ENABLING A BETTER WORLD
THROUGH CERAMIC AND GLASS MATERIALS
MONTREAL, CANADA
JULY 14–18, 2024 | HOTEL BONAVENTURE

Register now!

An American Ceramic Society Conference

ACerS INTERNATIONAL

ICF International Ceramic Foundation

ceramics.org/ICC2024